IEEE *Access*

RESEARCH ARTICLE

UAS-Based SAR Repeat-Pass Interferometry With Ground Truth

ALESSANDRA BENI, (Member, IEEE), **LAPO MICCINESI**, (Member, IEEE),
LORENZO PAGNINI, (Member, IEEE), **LUCA BIGAZZI, ANDREA CIONCOLINI**,
AND MASSIMILIANO PIERACCINI, (Member, IEEE)
Department of Information Engineering (DINFO), University of Florence, 50139 Florence, Italy

Corresponding author: Alessandra Beni (alessandra.beni@unifi.it)

ABSTRACT Radar systems operating aboard unmanned aerial systems (UASs) or drones are gaining lot of interest in the remote sensing field. UASs have recently been tested as platforms for synthetic aperture radar (SAR) systems. There are many expectations regarding the interferometric capabilities of UAS-based radar interferometers. Nevertheless, its implementation introduces new problems, which demand advanced processing techniques. To date, only few works presented interferometric data acquired aboard UAS. In this paper repeat-pass interferometric tests are presented, performed with an S-band UAS-based SAR. By using corner reflectors subject to known displacements, the interferometric capabilities of the sensor are demonstrated. Results from two measurement campaigns are presented: data acquired in controlled scenario and in a vegetated slope. A focusing algorithm that considers the UAS position and attitude information, able to cope with the UAS instabilities, is presented and discussed. At the knowledge of the authors, the experimental results obtained are the first systematic demonstration of repeat-pass UAS-based SAR interferometry, validated by ground truth.

INDEX TERMS Interferometric SAR, synthetic aperture radar, UAS, UAS-based SAR.

I. INTRODUCTION

Synthetic Aperture Radar (SAR) interferometry [1] is a powerful tool largely used in remote sensing applications. It exploits radar acquisitions along a certain aperture in order to form two dimensional images, and allows to measure displacements in the scenario, with sub-wavelength precision. The SAR systems were initially designed for satellite operations [1] in the sixties. Later, also airplanes [2] and ground-based (GB) actuators [3] have been used as SAR platforms, and today they are popular established sensors for environmental monitoring.

Today, unmanned aerial systems (UASs), commonly known as drones, are becoming ever more popular as platforms for SAR systems [4], [5], [6], [7], [8], [9], [10]. UASs allow for high flexible synthetic apertures (SA), and can be easily deployed without the need for complex launch infrastructures such as satellite, or fixed installation such

as GB-SAR. UAS-based SAR systems could bridge the gap between space-borne and GB-SAR. Indeed, they have short return times and allow to cover wide areas, up to tens of kilometers. Furthermore, such systems have a low cost compared to airborne SAR.

Performing UAS-based SAR imaging could be really challenging. Unlike satellite or GB actuators, UASs are usually subject to uncontrolled movements caused by external forces, such as wind gusts, which can make the UAS deviate from the nominal trajectory. These movements are usually called motion errors. They have been thoroughly studied for airborne SAR, and advanced algorithms have been proposed [11], [12], [13], [14]. To correctly focus SAR data in presence of motion errors, accurate knowledge of the radar antenna position and platform attitude as well as knowledge of the altitude profile of the illuminated area, are demanded. Back-propagation algorithms allow to cope with these problems, provided the knowledge of the UAS position.

Imaging techniques have been studied to perform motion compensation specifically for UAS-based systems [15], [16].

The associate editor coordinating the review of this manuscript and approving it for publication was Gerardo Di Martino.

Several works propose autofocusing algorithms to perform high resolution imaging [7], [17], [18]. Not all autofocus methods preserve the phase information and can be used for interferometric applications [8]. Autofocus methods capable of preserving image coherence have recently been presented [19]. However, these algorithms usually have long computation times, which can make their use difficult or limited. In many cases, back-propagation algorithms are used to focus UAS-based SAR images [8], [9], [20], [21].

The motion errors also affect the phase of the image. Consequently, they represent one of the main challenges in UAS-based interferometric SAR. In recent years, works addressing UAS-based SAR interferometry have appeared in scientific literature.

The possibility to perform single-pass interferometry has been successfully demonstrated in [22]. The authors presented results of single-pass interferometry using a P-band UAS-borne system. They estimated the terrain height of a eucalyptus forest with 5% accuracy.

Recently, also repeat-pass interferometry has been presented. Authors of [8], [21], [23], and [24], presented interferometric maps of realistic scenarios. Specifically, authors of [8] presented an X-band system. They observed severe image defocusing due to the platform deviation from the nominal trajectory and to the flight instabilities. Therefore, only small SA were used to process the interferometric measurements. The other works preferred lower frequencies than the X-band, as they are more suitable to preserve the phase coherence. In [21] and [23] a compact FMCW L-band UAV-borne system was used. Repeat-pass interferograms of a natural slope obtained with a short (5 min), and long (43 days) temporal baseline are showed. Authors of [24] used an S-band system and showed an interferometric map acquired in a urban scenario. Results obtained in the above works are really promising. However, the obtained interferometric maps were not confirmed by ground truth.

The first repeat-pass interferometric test onboard UAS, with ground truth validation was presented in [25]. Three corner reflectors were subject to known displacements. The L-band UAS-borne system measured vertical displacements in the scenario. Two interferometric measurements are presented. Obtained results have uncertainties close to the state of the art of satellite SAR, below 1 cm. Although this result represents an important step for UAS-based interferometry, only two measurements were presented, in a specific controlled scenario.

In this paper, repeat-pass interferometric measurements performed with a UAS-based SAR are presented. The system is an S-band radar, based on a vector network analyzer which operates aboard a UAS Matrice300RTK by DJI. The system was tested in different measurement campaigns. In this paper, a back-propagation focusing algorithm, originally developed for airborne SAR [14], is presented and adjusted to the UAS-based case. With respect to previous works, a time series of flight scans was performed in the same conditions, in order to test the measurement repeatability. The system was tested

in two different scenarios: a controlled scenario, and a natural one. The UAS performed linear flight scans at constant velocity. Corner reflectors were used as reference targets. In order to provide a reference for validation of the method, the corner reflectors were subject to known displacements. This allowed to test the reliability of the results obtained.

The paper is structured as follows: the UAS-based prototype for interferometric applications is presented in section II; the algorithm used to coherently focus SAR images is presented in section III; here the interferometric technique is also introduced and the possible error sources are discussed. Then, the experimental results obtained are presented and discussed in section IV.

II. UAS-BASED INTERFEROMETRIC SAR: EQUIPMENT

The payload for the UAS-based interferometric system is composed by the radar and the onboard computer. A block-scheme of the system architecture is shown in Fig. 1.

The onboard computer hosts the Robot Operating System (ROS) [26], a widely used framework for robotic applications. It allows to simultaneously manage and schedule operations on different hardware, and to enable their communication. In this case, ROS manages the communication with the UAS as well as the radar data acquisition.

The radar is based on a vector network analyzer (VNA) SC5065, by Copper Mountain, which provides a step frequency continuous wave (SFCW) signal from f_0 by steps of Δf. The m-frequency sample is given by $f_m = f_0 + (m-1)\Delta f$, $m = 1, \ldots, N_f$, with N_f the total number of frequency steps. The bandwidth of the signal is $B = N_f \Delta f$. Each tone is held for a time Δt. The VNA detects the in-phase and quadrature terms. Therefore, the acquired radar echo is a complex matrix E_{mn}, whose indexes $m = 1, \ldots, N_f$ and $n = 1, \ldots, N_n$ label the frequencies and the sweeps, respectively.

The sensor is equipped with a couple of log periodic antennas Hyper LOG6080 by Aaronia AG, Germany. The antennas have beamwidth of about 60° both in the horizontal and vertical plane. The received signal is amplified with a low
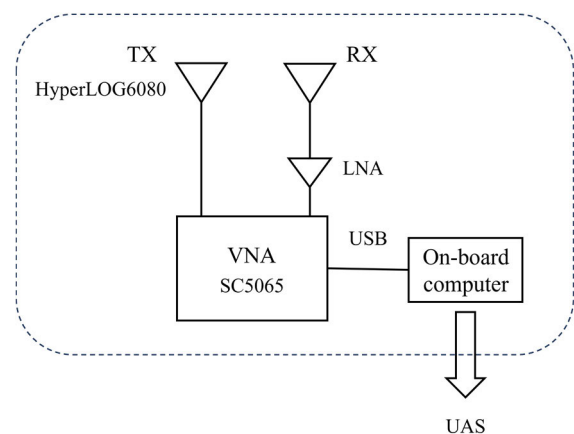

FIGURE 1. Block-scheme of the radar payload for the interferometric UAS-based SAR.

noise amplifier (LNA) a Mini-Circuits ZX60 - 63GLN+ with 29.6 dB of gain and sent to the VNA for demodulation. The VNA is connected to the onboard computer, which manages the radar operations and records the acquired data, via USB.

For the present experimentation the VNA provided a SFCW signal with central frequency f_c = 4.05 GHz and about $B \simeq 100$ MHz of bandwidth. The number of frequency steps was $N_f = 201$. For this configuration, the VNA allowed a maximum pulse repetition frequency (PRF) of 60 Hz. This imposed a limit on the UAS velocity. In fact, to properly focus SAR data without introducing angular ambiguity, the spatial step between successive acquisitions must be equal or smaller than $\lambda/4$ [27]. A flight speed of 1 m/s was suitable for the present experimentation. Although, with such a low velocity, a Doppler shift must be considered and compensated for. Indeed, in these conditions the following expression does not hold, $v/\lambda \gg$ PRF. It has been shown [28] that, in this case, the Doppler shift can not be considered negligible, and must be corrected. This was taken into account in the focusing algorithm explained in the following section.

III. UAS-BASED INTERFEROMETRIC SAR: METHODS
A. FOCUSING ALGORITHM
For the present work, a time-domain back-propagation algorithm based on [14], originally developed for airborne SAR, was used and generalized to the UAS-based case. A scheme of the acquisition geometry is shown in Fig. 2. Assume the UAS-based radar is in position $\mathbf{R_n}$ at time t_n. The target is in position $\mathbf{T}$. The vector $\mathbf{D_n}(\mathbf{T}) = \mathbf{T} - \mathbf{R_n}$ represents the position of the target with respect to the radar, at time t_n.
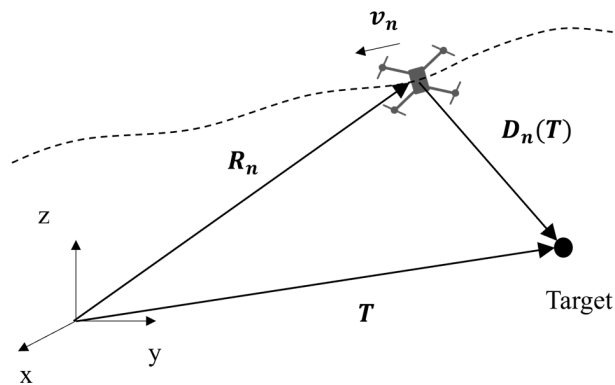

FIGURE 2. UAS-based acquisition geometry.

As already mentioned, because of the low PRF, a Doppler correction must be considered. The algorithm in [14] was then modified based on the methods described in [28], to account and compensate for the Doppler effect.

The SAR image $I(\mathbf{T})$ of a target in position $\mathbf{T}$ can be obtained from the radar complex echo E_{nm}, as [14],

$$I(\mathbf{T}) = \sum_{m=1}^{N_f} \sum_{n=n_1}^{n_2} E_{mn} e^{j\frac{4\pi}{c}f_m\left(D_n(\mathbf{T})+D_{mn}^{Dopp}\right)}. \quad (1)$$

Here, n is an index labelling the sweep acquisitions, j is the complex unit, c is the speed of light, f_m is the m-frequency sample, $D_n(\mathbf{T})$ is the module of vector $\mathbf{D_n}(\mathbf{T})$, and D_{mn}^{Dopp} is the Doppler compensation for the $m-$ th frequency sample, at time t_n. Indexes n_1 and n_2 delimit the summation over n, i.e. they define the processed synthetic aperture (PSA). According to [28] the Doppler term is given by,

$$D_{mn}^{Dopp} = m\Delta t \mathbf{v_n} \cdot \mathbf{D_n}(\mathbf{T}), \quad (2)$$

where $\mathbf{v_n}$ is the UAS velocity at time t_n.

To focus the SAR images, (1) was implemented on a grid defined on the ground, based on the flight trajectory. An example of the focusing geometry is shown in Fig. 3. The x-axis is parallel to the average flight direction. For each (x, y) point on the grid, the PSA (indexes n_1, n_2) was selected as the intersections with the flight trajectory, determined by an angle θ, as showed in Fig. 3. The maximum value of θ is the antenna beamwidth θ_{ant}. Indeed, for each antenna position, the radar illuminates an area delimited by $\theta = \theta_{ant}$. Therefore, for each target $\mathbf{T}$, only the contributions such that $\mathbf{T}$ is inside the antenna lobe should be considered. Such an implementation permits to modify θ, i.e. n_1, n_2, according to the UAS attitude. For instance, if the radar is not pointing perpendicular to the direction of flight, the PSA can be adjusted accordingly. In what follows, the angle θ will be called focusing angle.
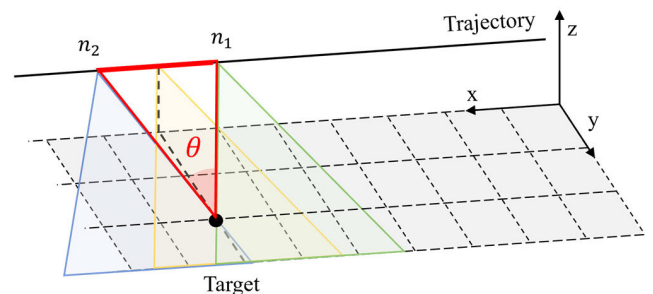

FIGURE 3. Scheme of the focusing geometry.

Given the high computational cost of (1), the approximation described in [28] was used, which considers the Doppler correction and uses the fast Fourier transform and an interpolation method in the range direction. In what follows, Kaiser windows (with $\beta = 5$) were also applied to the radar echoes, in range and cross-range directions, for lowering the sidelobes.

The coherent focusing of SAR data using (1) requires accurate knowledge of the UAS position $\vec{R}_n$. UAS are usually equipped with inertial measurements units (IMUs) and real time kinematic global positioning satellite systems (GNSS-RTK), which provide the UAS position information and attitude. In general, GNSS-RTK sensors allow accuracy of the order of centimetres. Positioning uncertainty can cause defocusing of SAR images: the main peak splits into several contributions [15], causing also a decrease in signal-to

noise-ratio. System working at lower frequencies, i.e. longer wavelengths, can bear higher position uncertainties and are less affected by defocusing effects.

B. UAS-BASED SAR INTERFEROMETRY

Once the SAR images have been focused on the same focusing grid, interferometric techniques [29] can be applied on the time series of the images. Given two images $I_a(x, y)$ and $I_b(x, y)$ acquired during two different scans, the interferometric phase can be computed for each target as the phase difference of the complex values, i.e.

$$\Delta\varphi(x, y) = \text{angle}(I_a(x, y) \cdot I_b(x, y)^*), \qquad (3)$$

where $\text{angle}(\cdot)$ denotes the phase of the complex value and $(\cdot)^*$ the conjugate. The phase difference, $\Delta\varphi$, can be related to a displacement of the scenario as

$$\Delta d = \frac{\lambda}{4\pi}\Delta\varphi, \qquad (4)$$

where λ is the wavelength corresponding to the central frequency of the radar signal.

Actually, the interferometric phase $\Delta\varphi$ contains several contributions:

$$\Delta\varphi = \Delta\varphi_{\text{disp}} + \Delta\varphi_{\text{atmo}} + \Delta\varphi_{\text{vol}} + \Delta\varphi_{\text{noise}}. \qquad (5)$$

Here, $\Delta\varphi_{\text{disp}}$ is the term due to the physical displacement of the target occurred between the two scans; $\Delta\varphi_{\text{atmo}}$ is the phase difference due to a change in the atmospheric refraction index between the acquisitions; $\Delta\varphi_{\text{vol}}$ is the volumetric contribution due to the fact that successive scans do not perfectly retrace the same trajectory; finally, $\Delta\varphi_{\text{noise}}$ is a noise term.

In order to measure only the physical displacement with (4), all other terms must be compensated or minimized, since they introduce errors that can compromise the interferometric measurement. The atmospheric contribution $\Delta\varphi_{\text{atmo}}$ can be compensated using specific algorithms [30], [31], [32], [33]. Usually, in typical natural measurement scenarios it is performed assuming a linear (or quadratic) range contribution. The volumetric phase $\Delta\varphi_{\text{vol}}$ is related to the non-perfect retracing during the repat-pass. To correct this contribution, a DEM as well as information on the UAS position are required. However, if all targets are located at the same altitude, i.e. they belong to the same horizontal plane, the volumetric phase can be compensated as it was an atmospheric contribution.

The noise term ($\Delta\varphi_{\text{noise}}$) cannot be completely eliminated. It includes all terms that contribute to the phase uncertainty (e.g. thermal noise, temporal and spatial decorrelation, focusing errors). In optimal situations, for satellite or GB-SAR, this term is negligible with respect to the other phase contributions ($\Delta\varphi_{\text{disp}}, \Delta\varphi_{\text{atmo}}, \Delta\varphi_{\text{vol}}$). In case of a UAS-based system, the noise term can be dominated by the uncertainty on the UAS position $\vec{R}_n$. The position errors enter the focusing algorithm (1), introducing uncertainty on the phase values of the radar image. A possible solution to minimize the effects of the positioning uncertainty on the interferometric phase,

is to lower the PSA. In (1) the PSA is determined by the focusing angle θ through the p_1, p_2 indexes, as schematically shown in Fig. 3. If the position is affected by noise, as the PSA increases, the more noise is added to the exponential term in (1). Considering an angle $\theta < \theta_{\text{ant}}$, i.e. shortening the PSA, it is possible to mitigate the effects of noise. How much the focusing angle θ influences the image quality, depends on the specific measurement conditions and on the positioning sensor uncertainty. Consequently, the optimal choice of focusing angle may vary from case to case.

Summing up, the phase contributions that are critical for interferometric applications are the volumetric contribution $\Delta\varphi_{\text{vol}}$ and the noise term $\Delta\varphi_{\text{noise}}$. Knowledge of a DEM of the area allows to correct the volumetric one. On the other hand, the phase uncertainty is linked to the positioning sensor uncertainty and could represent a limit for the coherence of SAR images.

IV. EXPERIMENTAL TESTS

The UAS system used for this experimentation was a commercial quadcopter, a Matrice300RTK, by DJI. It is equipped with IMU and RTK sensors. Fig. 4 shows a picture of the radar payload mounted onboard the UAS. The antennas are mounted on a support of 1 m length, in order to minimize the direct coupling.
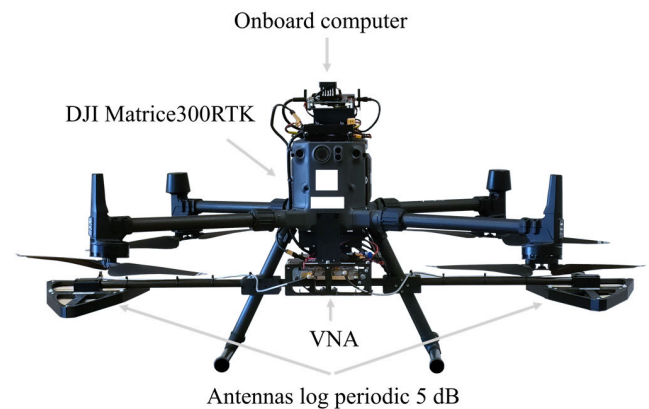

FIGURE 4. Picture of the UAS-based interferometric prototype.

In what follows, experimental results obtained in two measurement campaigns are presented and discussed. The first was performed in controlled scenario, in a general aviation airfield; the second was performed in a natural environment, the area of an ex-quarry.

A. TESTS IN CONTROLLED ENVIRONMENT

The equipment was first tested in the general aviation airfield of Serristori, Arezzo, Italy.

Measurements were performed using corner reflectors (CRs) as reference targets, in order to test and validate the measurement procedure and focusing algorithm. Three CRs of 50 cm side were positioned in a meadow area, mounted on tripods, at the same altitude on the ground. During the

measurements the UAS flew at 5 m altitude, with a velocity of 1 m/s. Nine scans were performed on the same nominal trajectory. The bandwidth of the radar signal was set equal to $B = 100.5$ MHz, which corresponds to a range resolution of about 1.5 m. Fig. 5 shows a picture of the UAS performing the measurement scan. Circles highlight the locations of the CRs. Between each flight, CR 2 (red in Fig. 5) was moved in the direction perpendicular to the scan line, by steps of 1 cm length. The position of the other two CRs was kept unchanged. Fig. 6 shows an aerial view of the imaged area, the UAS trajectory, and locations of the CRs.
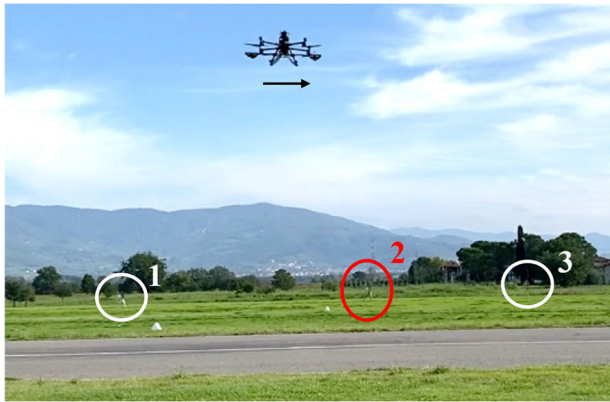

FIGURE 5. UAS-based SAR flight during the experiments at Serristori.
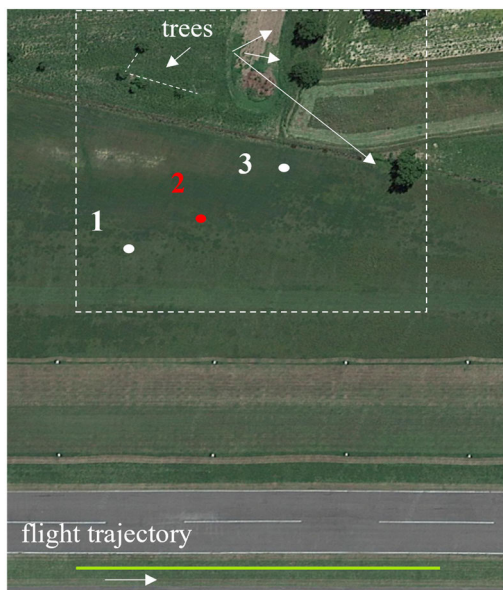

FIGURE 6. Aerial view of the imaged area in Fig. 7.

Radar raw data were focused using (1) and the result is shown in Fig. 7. The three CRs are clearly recognizable in the image. The trees, indicated by white arrows in Fig. 6 and Fig. 7, are also visible in the radar image.

As already mentioned, residual uncertainties on the UAS position R_n should affect the image quality, in particular, the
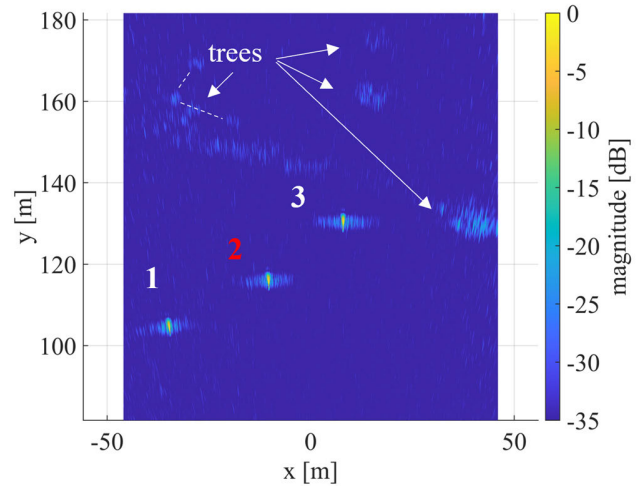

FIGURE 7. SAR image obtained using (1).

phase coherence. In order to better understand the effect of a different PSA in (1), the value of the focusing angle θ was varied, from $2°$ to $60°$. Fig. 8 shows the magnitude point spread function of CR 2 normalized with respect to the sweeps number in the processed synthetic aperture, obtained with different values of θ. By increasing θ, i.e. considering a longer PSA, the peak width becomes narrower. It is worth noting that the CR amplitude image is of good quality, even for $\theta = \theta_{ant} = 60°$, the whole antenna aperture. No defocusing of the image is observed. This means that positioning errors are not critical for image focusing in this frequency band.
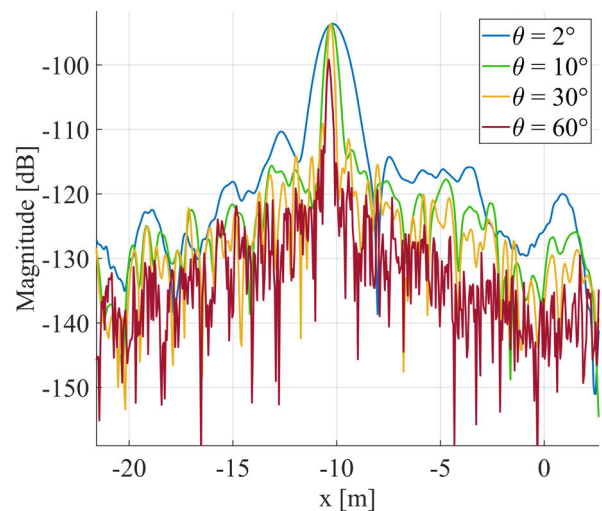

FIGURE 8. Magnitude PSF of CR 2 obtained with $\theta = 2°, 10°, 30°, 60°$.

Complex data of the three CRs were processed using interferometric techniques. As already mentioned, for targets at the same altitude, both the volumetric and the atmospheric phase contributions can be compensated for. A constant plus a linear range contribution was assumed and a correction

of $\Delta\varphi_{atmo}$ and $\Delta\varphi_{vol}$ was carried out, based on CR 1 and CR 3. For each image, the signal phase of the fixed CRs was used to estimate the range-linear phase contribution. The retrieved linear phase plane was then used to correct the signal phase of each pixel of the radar image, included CR 2. The interferometric displacement is then computed with (4) using the corrected phase.

In order to characterize the interferometric performance of the system, the root mean square error (RMSE) of the displacement of CR 2 with respect to the expected one ($d_{exp} = 0.01$ m) was evaluated,

$$\text{RMSE} = \sqrt{\frac{1}{N_{meas}} \sum_{i=1}^{N_{meas}} \left(d_i - d_{exp}\right)^2}. \qquad (6)$$

Here, d_i is the i-th measured displacement, and N_{meas} is the total number of measurements.

The computation was performed for several values of the focusing angle, from $\theta = 2°$, to $\theta = 60°$. Fig. 9 shows the RMSE obtained, as a function of the corresponding focusing angle. High measurement accuracy is achieved, with RMSE always below 2.5 mm, that is, below $\lambda/30$. For very small θ values, between 2° and 7°, the RMSE decreases from 2.4 mm down to 0.9 mm, reaching an even higher measurement precision. However, by further widening the synthetic aperture, the error increases. For $\theta = 60°$ it is about 1.7 mm. This behaviour can be explained as follows: by enlarging the PSA, more data are integrated and contribute to the result, leading to a better signal-to-noise-ratio. On the other hand, the position is affected by bias and uncertainties, and the more data are added, the more phase uncertainty is introduced. The curve in Fig. 9 results from a trade-off between these two aspects. Obtained results show that very high accuracy is obtained with a limited PSA. For the present case, using $\theta = 7°$ (PSA at 120 m of about 15 m) guarantees the maximum accuracy, a RMSE of 0.9 mm. The curve in Fig. 9
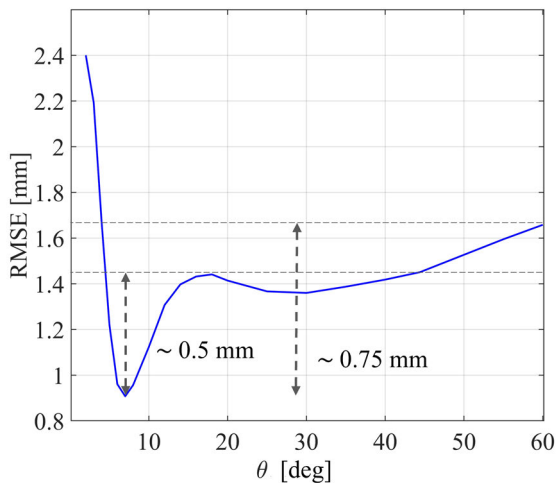
suggests that a further increase of the focusing angle does not provide significant advantages. Therefore, it would be suitable to use $\theta < \theta_{ant}$. Indeed, this lowers the computational cost and accelerates the focusing process.

Fig. 10 shows the interferometric displacement obtained for the three CRs, with $\theta = 7°$. Here, the measured cumulative interferometric displacement is shown as a function of the nominal displacement expected for CR 2. It can be observed that the displacement of CR 2 before the correction (blue line in Fig. 10) overestimates the expected result. On the other hand, after the atmospheric and volumetric contributions have been corrected, the displacement of CR 2 (red line) better agrees with the expected trend. Very good agreement can be observed, with a maximum deviation from the expected value of 2 mm.
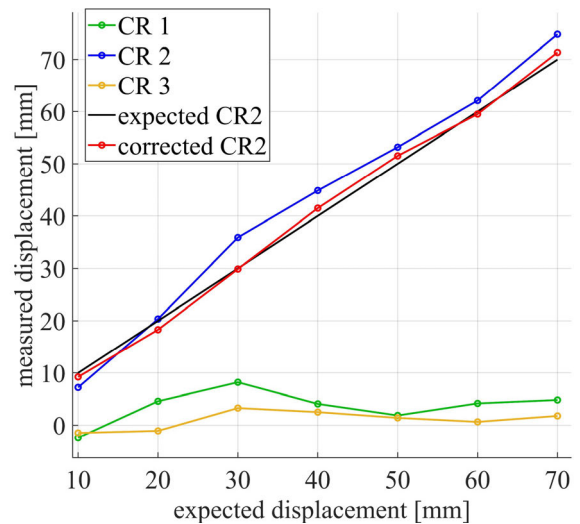

FIGURE 10. Measured cumulative interferometric displacements as a function of the expected displacement for CR 2. The green line is related to CR 1, blue line to CR 2, yellow line to CR 3, and red line to CR 2 after the correction implemented using the fixed CRs.

The millimetric accuracy achieved on CRs is consistent with that of state of the art satellite [34] and airborne [35] systems. Therefore, the presented results demonstrate the feasibility of UAS-based SAR interferometry.

B. TESTS IN NATURAL SCENARIO
A second experimental campaign was performed in an ex-quarry area, near Firenzuola, Italy. The illuminated area was a partially vegetated slope with rocks of various size. A CR was positioned on the slope. Fig. 11 shows a picture of the illuminated area and the CR position. A top view of the area is shown in Fig. 12. Here, the CR is highlighted by a white dot and the green line outlines the flight trajectory of the UAS.

Twelve flight scans were performed. The UAS flew following a straight trajectory about 45 m long, at about 20 m altitude, approximately the same altitude as the CR position. The velocity was equal to 1 m/s. The present scenario demanded a maximum unambiguous range of 450 m, which
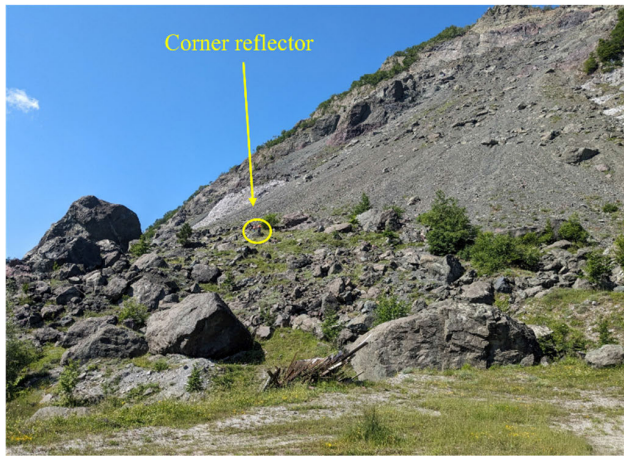

FIGURE 9. Root mean square error of the interferometric displacement with respect to the expected one, as a function of the angle θ used for focusing.

FIGURE 11. Picture of the slope scanned with the UAS-based system. The yellow circle highlights the CR position.
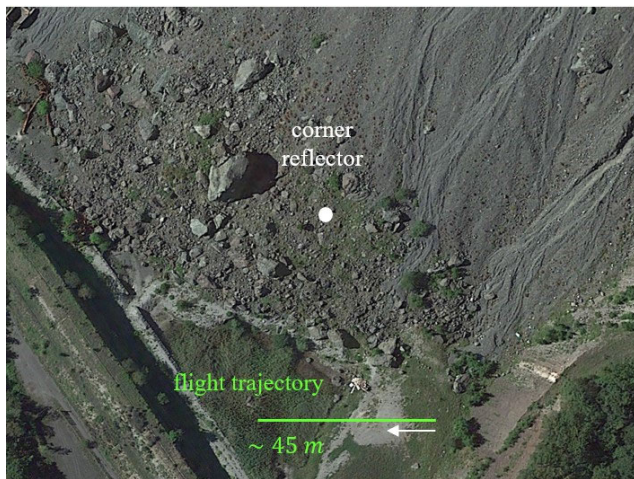

FIGURE 12. Top view of the UAS trajectory and location of the CR.

determined a bandwidth $B = 67$ MHz. The resulting range resolution was about 2.3 m.

As done in the previous tests, between each scan, the CR was moved by constant steps in the direction perpendicular to the scan line. In this case the displacements were 5 mm long.

Compared to the campaign presented above, in this case the measurement conditions were really challenging. Indeed, there were moderate wind gusts, that made the UAS partially deviate from the nominal linear trajectory. In addition, the area was characterized by a very steep and irregular slope and high-resolution DEM of the area was not available. The lack of DEM information is not dramatic in this case, as the UAS flew approximately at the same height of the CR. However, given the highly irregular shape of the slope, without a high resolution DEM it was not possible to implement the atmospheric phase correction, nor the volumetric one.

The poor range resolution was an additional source of noise. In fact, signals from different targets fall into the same resolution cell. This is also the case with the CR: targets in
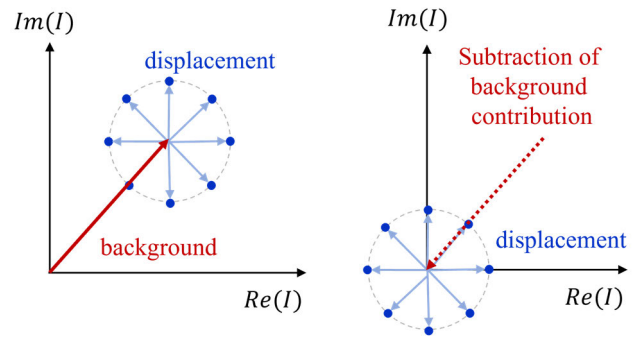

FIGURE 13. Procedure to remove the background contribution.

the surrounding environment are summed to the CR signal. The resulting signal is given by a background signal plus the CR signal. The CR was located near to a large stone. Therefore, the main background contribution is given by a constant clutter. A constant displacement of the target corresponds to a rotation of the signal phasor in the complex plane. If no background signal were present, the measured values would form a circle in the complex plane, around the origin [36]. The constant background translates this circle, leading to a possible underestimation of the interferometric phase. In order to cope with this problem, the following strategy was adopted: on the complex plane, the centre of the circle given by the CR complex phasors was estimated, which provides an estimate of the average background contribution. Then, such a contribution was subtracted from the CR signal. This procedure is schematically shown in Fig. 13, and an example of the procedure applied to experimental data is shown in Fig. 14.
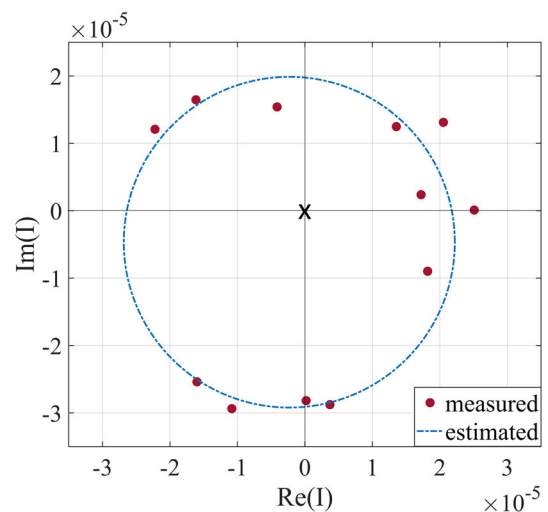

FIGURE 14. Estimation of the circle identified by the CR signals in the complex plane for the removal of the background contribution.

Fig. 15 shows the interferometric displacement of the CR obtained with $\theta = 2°$ (PSA$\simeq$ 2.79m) and $\theta = 20°$ (PSA $\simeq$ 28.2m), after the correction of the background contribution.
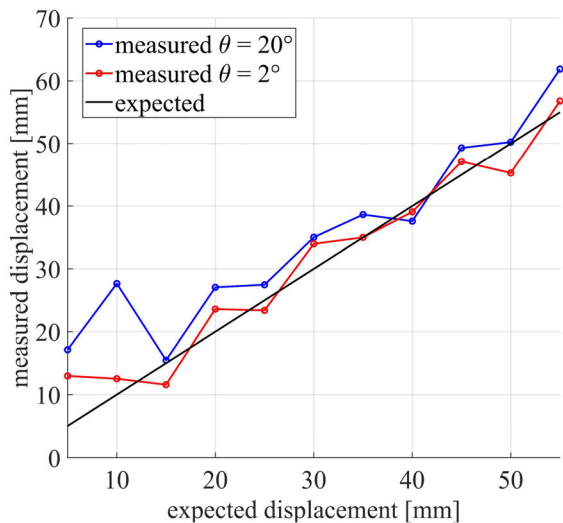
FIGURE 15. Measured cumulative interferometric displacements as a function of the expected displacement, obtained with $\theta = 2°$ (red) and $\theta = 20°$ (blue).
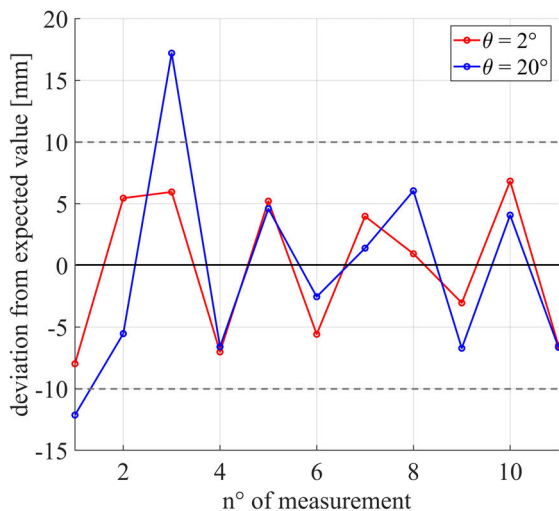

FIGURE 16. Deviation of the measured displacements from the expected value for $\theta = 2°$ (red), and $\theta = 20°$ (blue).

Measured data outline a clear trend, similar to the expected one. The RMSE obtained with $\theta = 20°$ is equal to 7.9 mm. A better agreement can be observed for $\theta = 2°$, for which a RMSE of 5.7 mm was measured. Fig. 16 shows the deviations of the measured displacements from the expected values. For $\theta = 2°$, the deviations are always below 1 cm. For values of θ larger than 20° the errors increase, and make the cumulative displacement slightly deviate from the expected one. Given the challenging measurement conditions and the lack of atmospheric and volumetric corrections, the results obtained are extremely promising. Indeed, for short PSA, the displacements were determined with errors lower than 1 cm, a precision very close to that achievable with C and X-band spaceborne and airborne systems [25], [34], [35].

V. CONCLUSION

UAS-based radar interferometry is a promising tool which is raising lot of interest. To date, no systematic studies have been conducted on interferometric data acquired onboard UASs.

In this paper, repeat-pass interferometry on UAS-based SAR data was demonstrated. A back-propagation algorithm for image focusing, originally developed for airborne SAR, has been generalized for UAS-based systems. A method able to compensate for a Doppler shift is implemented. Considering the information on the position and attitude of the UAS, the algorithm allows to cope with the UAS instabilities. The possible sources of noise in the interferometric phase were outlined and the methods for their correction were discussed.

Measurements performed on corner reflectors in controlled scenario were presented. Several flight scans were performed in the same conditions, in order to test the measurement repeatability and reliability. A corner was moved by known displacements between each flight scan. This provided a reference for validation of the method. It was shown that uncertainties in the UAS position are not critical in S-band, as the CR image was not subject to defocus. The interferometric displacement of a corner reflector was corrected using information from other two fixed corner reflectors. The root mean square error of the measured displacements was evaluated as a function of the synthetic aperture used for focusing. It was shown that millimetric precision can be achieved. The obtained displacement showed excellent agreement with the expected result, in line with that of other state-of-the-art interferometric systems.

One other acquisition campaign was performed in the area of an ex-quarry, a natural, partially vegetated slope. Interferometric measurements were carried out on a corner reflector located on the slope. In this case, the measurement conditions were challenging: the slope was irregular and no DEM was available, the system had poor range resolution, and moderate wind gusts were present (about 6 - 7 m/s). In this case the interferometric results appear noisier than in controlled scenario. This is probably due to a combination of factors previously mentioned. For instance, it was not possible to compensate for the volumetric phase contribution because of the lack of a high-resolution DEM. Nevertheless, also in this case, interferometry was performed successfully and good agreement with the expected result was found. The achieved measurement precision on the corner reflector, below 1 cm, is comparable to that of state-of-the-art interferometers.

It must be underlined that knowledge of DEM is fundamental to perform interferometric measurements on natural slopes landslides.

The millimetric accuracy of the presented results on corner reflectors demonstrates the possibility to successfully apply the interferometric technique to UAS-based SAR data. The dataset presented demonstrates the repeatability and reliability of the method. The study presented in this paper poses the first steps of interferometric UAS-based SAR implementations, showing the potential and outlining the main challenges.

To further improve the system performance more measurement campaigns will be carried out in different meteorological conditions and different scenarios. Furthermore, UAS-based SAR interferometric processing could benefit from the application of coherence maximization or autofocus methods to minimize the phase errors.

REFERENCES

[1] A. Moreira, P. Prats-Iraola, M. Younis, G. Krieger, I. Hajnsek, and K. P. Papathanassiou, "A tutorial on synthetic aperture radar," *IEEE Geosci. Remote Sens. Mag.*, vol. 1, no. 1, pp. 6–43, Mar. 2013, doi: 10.1109/MGRS.2013.2248301.

[2] A. L. Gray and P. J. Farris-Manning, "Repeat-pass interferometry with airborne synthetic aperture radar," *IEEE Trans. Geosci. Remote Sens.*, vol. 31, no. 1, pp. 180–191, Jan. 1993, doi: 10.1109/36.210459.

[3] Y. Wang, W. Hong, Y. Zhang, Y. Lin, Y. Li, Z. Bai, Q. Zhang, S. Lv, H. Liu, and Y. Song, "Ground-based differential interferometry SAR: A review," *IEEE Geosci. Remote Sens. Mag.*, vol. 8, no. 1, pp. 43–70, Mar. 2020, doi: 10.1109/MGRS.2019.2963169.

[4] T. Deguchi, T. Sugiyama, and M. Kishimoto, "Development of SAR system installable on a drone," in *Proc. 13th Eur. Conf. Synth. Aperture Radar*, Mar. 2021, pp. 1–3.

[5] L. Miccinesi, A. Beni, and M. Pieraccini, "UAS-borne radar for remote sensing: A review," *Electronics*, vol. 11, no. 20, p. 3324, Oct. 2022, doi: 10.3390/electronics11203324.

[6] A. Carpenter, J. A. Lawrence, R. Ghail, and P. J. Mason, "The development of copper clad laminate horn antennas for drone interferometric synthetic aperture radar," *Drones*, vol. 7, no. 3, p. 215, Mar. 2023, doi: 10.3390/drones7030215.

[7] A. Bekar, M. Antoniou, and C. J. Baker, "Low-cost, high-resolution, drone-borne SAR imaging," *IEEE Trans. Geosci. Remote Sens.*, vol. 60, 2022, Art. no. 3085235, doi: 10.1109/TGRS.2021.3085235.

[8] M. Lort, A. Aguasca, C. López-Martínez, and T. M. Marín, "Initial evaluation of SAR capabilities in UAV multicopter platforms," *IEEE J. Sel. Topics Appl. Earth Observ. Remote Sens.*, vol. 11, no. 1, pp. 127–140, Jan. 2018, doi: 10.1109/JSTARS.2017.2752418.

[9] G. Oré, M. S. Alcântara, J. A. Góes, B. Teruel, L. P. Oliveira, J. Yepes, V. Castro, L. S. Bins, F. Castro, D. Luebeck, L. F. Moreira, R. Cintra, L. H. Gabrielli, and H. E. Hernandez-Figueroa, "Predicting sugarcane harvest date and productivity with a drone-borne tri-band SAR," *Remote Sens.*, vol. 14, no. 7, p. 1734, Apr. 2022, doi: 10.3390/rs14071734.

[10] A. Bekar, M. Antoniou, and C. J. Baker, "Change detection for high-resolution drone-borne SAR at high frequencies–first results," in *Proc. IEEE Radar Conf.*, May 2023, pp. 1–5, doi: 10.1109/RadarConf2351548.2023.10149798.

[11] A. Moreira and Y. Huang, "Airborne SAR processing of highly squinted data using a chirp scaling approach with integrated motion compensation," *IEEE Trans. Geosci. Remote Sens.*, vol. 32, no. 5, pp. 1029–1040, Sep. 1994, doi: 10.1109/36.312891.

[12] G. Fornaro, "Trajectory deviations in airborne SAR: Analysis and compensation," *IEEE Trans. Aerosp. Electron. Syst.*, vol. 35, no. 3, pp. 997–1009, Jul. 1999, doi: 10.1109/7.784069.

[13] J. Chen, M. Xing, H. Yu, B. Liang, J. Peng, and G.-C. Sun, "Motion compensation/autofocus in airborne synthetic aperture radar: A review," *IEEE Geosci. Remote Sens. Mag.*, vol. 10, no. 1, pp. 185–206, Mar. 2022, doi: 10.1109/MGRS.2021.3113982.

[14] P. Berardino, A. Natale, C. Esposito, R. Lanari, and S. Perna, "On the time domain airborne SAR focusing in presence of strong azimuth variations of the squint angle," *IEEE Trans. Geosci. Remote Sens.*, vol. 61, 2023, Art. no. 3289593, doi: 10.1109/TGRS.2023.3289593.

[15] P. Stockel, P. Wallrath, R. Herschel, and N. Pohl, "Motion compensation in six degrees of freedom for a MIMO radar mounted on a hovering UAV," *IEEE Trans. Aerosp. Electron. Syst.*, vol. 59, no. 5, pp. 5791–5801, Oct. 2023, doi: 10.1109/TAES.2023.3266181.

[16] Z. Lv, F. Li, X. Qiu, and C. Ding, "Effects of motion compensation residual error and polarization distortion on UAV-borne PolInSAR," *Remote Sens.*, vol. 13, no. 4, p. 618, Feb. 2021, doi: 10.3390/rs13040618.

[17] Z. Ding, L. Li, Y. Wang, T. Zhang, W. Gao, K. Zhu, T. Zeng, and D. Yao, "An autofocus approach for UAV-based ultrawideband ultrawidebeam SAR data with frequency-dependent and 2-D space-variant motion errors," *IEEE Trans. Geosci. Remote Sens.*, vol. 60, 2022, Art. no. 3062183, doi: 10.1109/TGRS.2021.3062183.

[18] W. Liu, H. Feng, and Y. Lu, "Ka-band drone SAR flying without GPS," in *Proc. 7th Asia–Pacific Conf. Synth. Aperture Radar*, Nov. 2021, pp. 1–4, doi: 10.1109/APSAR52370.2021.9688524.

[19] A. Bekar, M. Bekar, C. J. Baker, and M. Antoniou, "Coherent change detection for high-resolution drone-borne SAR at 24 GHz," *IEEE J. Sel. Topics Appl. Earth Observ. Remote Sens.*, vol. 17, pp. 84–94, 2024, doi: 10.1109/JSTARS.2023.3324570.

[20] L. Moreira, F. Castro, J. A. Góes, L. Bins, B. Teruel, J. Fracarolli, V. Castro, M. Alcântara, G. Oré, L. Luebeck, L. P. Oliveira, L. Gabrielli, and H. E. Hernandez-Figueroa, "A drone-borne multiband DInSAR: Results and applications," in *Proc. IEEE Radar Conf.*, Apr. 2019, pp. 1–6, doi: 10.1109/RADAR.2019.8835653.

[21] O. Frey, C. L. Werner, and R. Coscione, "Car-borne and UAV-borne mobile mapping of surface displacements with a compact repeat-pass interferometric SAR system at L-band," in *Proc. IEEE Int. Geosci. Remote Sens. Symp.*, Jul. 2019, pp. 274–277, doi: 10.1109/IGARSS.2019.8897827.

[22] L. Moreira, D. Lübeck, C. Wimmer, F. Castro, J. A. Góes, V. Castro, M. Alcântara, G. Oré, L. P. Oliveira, L. Bins, B. Teruel, L. H. Gabrielli, and H. E. Hernandez-Figueroa, "Drone-borne P-band single-pass InSAR," in *Proc. IEEE Radar Conf.*, Sep. 2020, pp. 1–6, doi: 10.1109/RadarConf2043947.2020.9266502.

[23] O. Frey and C. L. Werner, "UAV-borne repeat-pass SAR interferometry and SAR tomography with a compact L-band SAR system," in *Proc. 13th Eur. Conf. Synth. Aperture Radar*, USA, Mar. 2021, pp. 1–4.

[24] S.-Y. Jeon, B. Hawkins, S. Prager, M. Anderson, S. Moro, R. Beauchamp, E. Loria, S.-J. Chung, and M. Lavalle, "Uav-borne bistatic SAR and insar experiments in support of STV and SDC target observables," in *Proc. IEEE Int. Geosci. Remote Sens. Symp.*, Jul. 2023, pp. 1906–1909, doi: 10.1109/IGARSS52108.2023.10282077.

[25] D. Luebeck, C. Wimmer, L. F. Moreira, M. Alcântara, G. Oré, J. A. Góes, L. P. Oliveira, B. Teruel, L. S. Bins, L. H. Gabrielli, and H. E. Hernandez-Figueroa, "Drone-borne differential SAR interferometry," *Remote Sens.*, vol. 12, no. 5, p. 778, Feb. 2020, doi: 10.3390/rs12050778.

[26] (2023). *ROS: Home.* Accessed: Aug. 03, 2023. [Online]. Available: https://www.ros.org/

[27] M. Pieraccini, D. Tarchi, H. Rudolf, D. Leva, G. Luzi, G. Bartoli, and C. Atzeni, "Structural static testing by interferometric synthetic radar," *NDT E Int.*, vol. 33, no. 8, pp. 565–570, Dec. 2000, doi: 10.1016/s0963-8695(00)00027-x.

[28] A. Beni, L. Miccinesi, and M. Pieraccini, "UAS-borne CWSF SAR imaging: Evaluation and compensation of Doppler effect," in *Proc. IEEE Int. Radar Conf. (RADAR)*, Nov. 2023, pp. 1–5, doi: 10.1109/RADAR54928.2023.10371049.

[29] P. A. Rosen, S. Hensley, I. R. Joughin, F. K. Li, S. N. Madsen, E. Rodriguez, and R. M. Goldstein, "Synthetic aperture radar interferometry," *Proc. IEEE*, vol. 88, no. 3, pp. 333–382, Mar. 2000, doi: 10.1109/5.838084.

[30] Y. Deng, C. Hu, W. Tian, and Z. Zhao, "A grid partition method for atmospheric phase compensation in GB-SAR," *IEEE Trans. Geosci. Remote Sens.*, vol. 60, 2022, Art. no. 3074161, doi: 10.1109/TGRS.2021.3074161.

[31] F. Falabella, A. Perrone, T. A. Stabile, and A. Pepe, "Atmospheric phase screen compensation on wrapped ground-based SAR interferograms," *IEEE Trans. Geosci. Remote Sens.*, vol. 60, 2022, Art. no. 3055648, doi: 10.1109/TGRS.2021.3055648.

[32] Y. Izumi, G. Nico, and M. Sato, "Time-series clustering methodology for estimating atmospheric phase screen in ground-based InSAR data," *IEEE Trans. Geosci. Remote Sens.*, vol. 60, 2022, Art. no. 3072037, doi: 10.1109/TGRS.2021.3072037.

[33] R. Iglesias, X. Fabregas, A. Aguasca, J. J. Mallorqui, C. Lopez-Martinez, J. A. Gili, and J. Corominas, "Atmospheric phase screen compensation in ground-based SAR with a multiple-regression model over mountainous regions," *IEEE Trans. Geosci. Remote Sens.*, vol. 52, no. 5, pp. 2436–2449, May 2014, doi: 10.1109/TGRS.2013.2261077.

[34] M. Bonano, M. Manunta, A. Pepe, L. Paglia, and R. Lanari, "From previous C-band to new X-band SAR systems: Assessment of the DIn-SAR mapping improvement for deformation time-series retrieval in urban areas," *IEEE Trans. Geosci. Remote Sens.*, vol. 51, no. 4, pp. 1973–1984, Apr. 2013, doi: 10.1109/TGRS.2012.2232933.

[35] S. Perna, C. Wimmer, J. Moreira, and G. Fornaro, "X-band airborne differential interferometry: Results of the OrbiSAR campaign over the perugia area," *IEEE Trans. Geosci. Remote Sens.*, vol. 46, no. 2, pp. 489–503, Feb. 2008, doi: 10.1109/TGRS.2007.908871.

[36] M. Pieraccini, F. Papi, and N. Donati, "I-Q imbalance correction of microwave displacement sensors," *Electron. Lett.*, vol. 51, no. 13, pp. 1021–1023, Jun. 2015, doi: 10.1049/el.2015.0982.

LUCA BIGAZZI was born in Florence, Italy, in 1987. He received the B.S. degree in electronics engineering, the M.S. degree in electrical and automation engineering, and the Ph.D. degree in information engineering from the University of Florence, Florence, in 2013, 2017, and 2021, respectively.

He is currently a Postdoctoral Researcher with the Department of Information Engineering, University of Florence. His research interests include computer vision, sensor fusion, control systems, robotics, and autonomous navigation.

ALESSANDRA BENI (Member, IEEE) received the B.S. degree in physics, the M.S. degree in theoretical physics, and the Ph.D. degree in information engineering from the University of Florence, in 2016, 2019, and 2023, respectively.

She is currently a Postdoctoral Researcher with the Department of Information Engineering, University of Florence. Her research interests include ground-penetrating radar, ground-based synthetic aperture radar, radar interferometry, radar data processing, and UAS-based radars.

ANDREA CIONCOLINI was born in Florence, Italy, in May 1991. He received the M.S. degree in electronics engineering from the University of Florence, in October 2020, where he is currently pursuing the Ph.D. degree.

He worked for about three years in the industrial sector as a HW Designer of radar systems. His research interests include ground-based synthetic aperture radar, radar Interferometry, and UAS-based radars.

LAPO MICCINESI (Member, IEEE) received the B.S. degree in physics, the M.S. degree in physics of particles, and the Ph.D. degree in information engineering from the University of Florence, Florence, Italy, in 2011, 2016, and 2020, respectively.

Since 2023, he has been a Researcher with the Department of Information Engineering, University of Florence. His research interests include ground penetrating radar, radar interferometry, ground-based radar, and ground-based synthetic aperture radar. He was a recipient of Florence University Press Award, in 2020, for the seven Best Ph.D. theses defended at the University of Florence.

MASSIMILIANO PIERACCINI (Member, IEEE) received the B.S. degree in mechanical engineering from National Chung Cheng University, Chi-ayi, Taiwan, and the M.S. degree in physics and the Ph.D. degree in non-destructive testing from the University of Florence, Florence, Italy, in 1994 and 1998, respectively. He was a Research Assistant and an Associate Professor with the Department of Electronics and Telecommunications (former Department of Electronic Engineering), University of Florence. Since 2021, he has been a Full Professor with the Department of Information Engineering, University of Florence. He is currently the President of Electronic Engineering with the University of Florence. He is the author of more than 180 publications, and more than nine patents inventions. His research interests include ground penetrating radar, ground-based synthetic aperture radar, interferometric radar, and microwave sensors.

LORENZO PAGNINI (Member, IEEE) was born in Florence, Italy, in February 1991. He received the B.Sc. degree in electronic and telecommunications engineering, the M.Sc. degree in electronic engineering, and the Ph.D. degree in information engineering from the University of Florence, Florence, in 2016, 2019, and 2023, respectively. His defended the Ph.D. thesis on "Time-Varying Power-Series Analysis in the Design of Microwave Highly-Linear GaN Active Mixers and Pas."

He is currently a Postdoctoral Researcher with the Department of Information Engineering, University of Florence, where he works on the development of interferometric radars for ground instability monitoring.

● ● ●